

1 **Statistical characteristics of raindrop size**
2 **distribution during rainy seasons in Complicated**
3 **Mountain Terrain**

4 Wenqian Mao^{1,3,4}, Wenyu Zhang^{2,3,4}, Menggang Kou²

5 1. College of Resources and Environmental Sciences, Gansu Agricultural University, Lanzhou

6 730070, China

7 2. School of Geoscience and Technology, Zhengzhou University, Zhengzhou, 450001, China

8 3. Key Laboratory for Cloud Physics, Chinese Academy of Meteorological Sciences, Beijing

9 100081, China

10 4. College of Atmospheric Sciences, Lanzhou University, Lanzhou, 730000, China

11 Correspondence to: Wenqian Mao (mdycmwq@163.com)

12 **Abstract:** In order to improve understanding of the characteristics of raindrop size
13 distribution (DSD) over complex mountainous terrain, the differences in DSD over the
14 southern slopes, northern slopes and interior of the Qilian Mountains were analyzed
15 using six months of observations. For all rainfall events, the number concentrations of
16 small and large raindrops in the interior and on the southern slopes were greater than
17 on the northern slopes, but midsize raindrops were less. The DSD spectrum of the
18 interior was more variable and differed significantly from that of the northern slopes.
19 The differences in the normalized intercept parameters of the DSD for stratiform and
20 convective rainfall were 8.3% and 10.4%, respectively, and those of the mass-weighted
21 mean diameters~~mass-weighted diameters~~ were 10.0% and 23.4%, respectively, while
22 the standard deviations of DSD parameters at interior sites were larger. The differences
23 in the coefficient and exponent of the Z-R relationship were 2.5% and 10.7%,
24 respectively, with an increasing value of the coefficient from the southern to the
25 northern slopes for stratiform rainfall, but the opposite for convective rainfall. In
26 addition, the DSD characteristics and Z-R relationships were more similar at the
27 ipsilateral sites and had smaller differences between the southern slopes and interior of
28 the mountains.

29 **Keywords:** raindrop size distribution; complicated mountain terrain; spatial variation
30
31

32 1 Introduction

33 Raindrop size distribution (DSD), the number of raindrops per drop size per unit
34 volume, is an important parameter to statistically describe the microstructure of
35 precipitation (Bringi et al., 2003; Ma et al., 2019a). The measurement of DSD can
36 provide some fundamental information such as raindrop size (D), liquid water content
37 (W), rain rate (R), radar reflectivity factor (Z) and so on, which has an essential
38 contribution to improving quantitative precipitation estimation (QPE) using weather
39 radar and satellite observations (Adirosi et al., 2018; Jash et al., 2019). The
40 parameterization of DSD can obtain the distribution model parameters of DSD in
41 different rain types, which is significant in advancing microphysics parameterization in
42 numerical weather prediction (NWP) models (Wainwright et al., 2014; McFarquhar et
43 al., 2015; Zhao et al., 2019). In addition, understanding the DSD is crucial in many
44 applied fields concerning hydrology, agriculture, soil erosion and microwave
45 communication (Rincon et al., 2002; Smith et al., 2009; Angulo-Martínez et al., 2015;
46 Lim et al., 2015; Yang et al., 2016).

47 Numerous studies have been carried out on the statistical characteristics of DSD
48 in different regions (Campos et al., 2006; Seela et al., 2017; Dolan et al., 2018; Protat
49 et al., 2019; Loh et al., 2019; Jash et al., 2019). It has been shown that the number
50 concentration and size of raindrops increase with rain rate and so the DSD becomes
51 higher and wider. The characteristics in different rain types demonstrate that the mass-
52 weighted mean diameter (i.e., D_m) and normalized intercept parameter (i.e., N_w) of
53 convective rainfall are larger than those of stratiform rainfall. Furthermore, these
54 studies also reveal that there are more differences in the characteristics of DSD. Dolan
55 et al. (2018) divided global DSD characteristics into 6 types by using 12 datasets across
56 three latitudes and found that the centralized regions and DSD parameters of the 6 types
57 varied in location. The average number of raindrops in central Korea was usually
58 greater than that in the southeast under three rainfall systems, especially drops in the
59 0.31–0.81mm diameter range (Loh et al., 2019). According to DSD measurements in
60 the Tibetan Plateau region, eastern areas have a higher raindrop number concentration
61 in the diameter range of 0.437–1.625 mm and greater variation in diameters than in
62 central areas (Wang et al., 2020). Compared to eastern China and northern China, the
63 DSD in southern China shows a higher number concentration of relatively small-sized
64 drops (Zhang et al., 2019). Comparison of the Z - R relationship (defined as $Z=AR^b$)
65 indicates that the coefficient decreases with increasing R in the southern Tibetan Plateau,
66 which is opposite to the case in ~~southern~~South China (Wu et al., 2017). For the DSD
67 parameters of stratiform and convective rainfall, there are various changes between the
68 lower and middle reaches of the Yangtze River (Fu et al., 2020).

69 As reported in the above studies, DSD characteristics vary significantly with
70 factors such as geographical location, climatic region and rain types. Pu et al. (2020)
71 analyzed the DSD characteristics of five sites in Nanjing city and found the N_w of DSD
72 to be largest at site near industrial areas, but the D_m of DSD was largest at sites near the
73 city's center. In other words, even at the urban scale, there are still differences in the
74 microphysical characteristics reflected by the DSD, which is due to the influence of the
75 surrounding environment. How, then, do the characteristics of DSD vary from location

带格式的: 字体: 倾斜

带格式的: 字体: 倾斜

76 to location over the complicated mountain terrain? Rao et al. (2006), by comparing the
77 DSD parameters at different altitudes, suggested that the obvious variation in DSD with
78 altitude is related to the processes of evaporation and breakup. Using aircraft
79 observations, Geoffroy et al. (2014) concluded that the total concentration of raindrops
80 decreased while the average drop size increased with decreasing altitude. But how large
81 might the differences in DSD be at different altitudes in mountainous regions? And how
82 significant might the effects be of these differences?

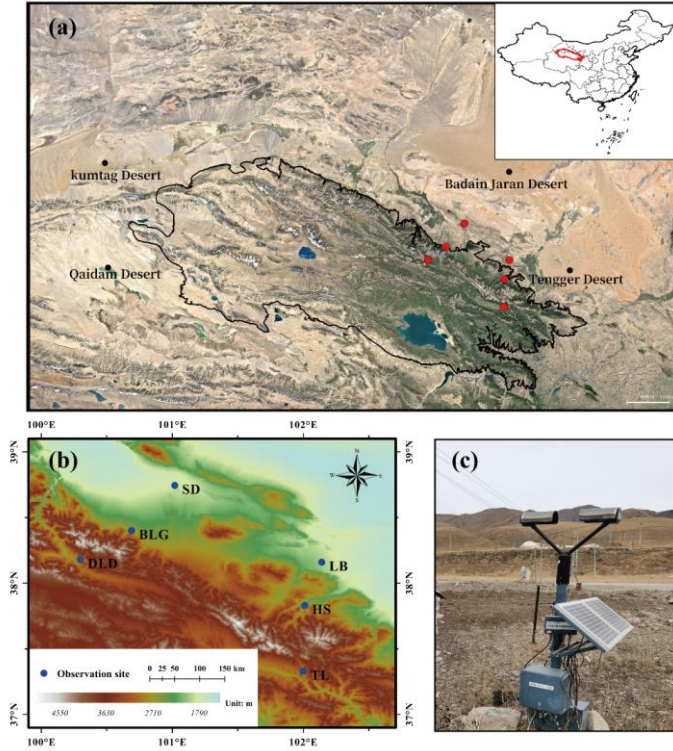
83 The Qilian Mountains, a series of marginal mountains in the northeastern part of
84 the Tibetan Plateau, are a vitally important ecological protection barrier in the northwest
85 arid areas of the region, that block the connection between deserts and wilderness
86 (Figure 1a). The mountains form several inland rivers that are important water sources
87 for the arid areas of the northwest and have therefore made a considerable contribution
88 to regional economic development (Gou et al., 2005; Tian et al., 2014; Qin et al., 2016).
89 In this study, we chose the Qilian Mountains as the research object and selected six sites
90 with different backgrounds representing the southern slopes, northern slopes and
91 interior of the mountains. To thoroughly investigate the discrepancies in this complex
92 mountain terrain, the DSD characteristics and $Z-R$ relationships were comprehensively
93 analyzed according to different rain types based on continuous disdrometer
94 observations in the rainy season. The primary goal was to obtain a deeper understanding
95 and characteristic differences of DSD over the Qilian Mountains and ~~refincimprove~~ the
96 accuracy of QPE, which could then be used as a research foundation for developing
97 cloud water resources in mountainous areas.

98 2 Data and method

99 2.1 Sites and instruments

100 The eastern and middle sections of the Qilian Mountains were chosen as the main
101 study area, taking into account that several important inland rivers originate from these
102 areas (Li et al., 2019). Six disdrometers were deployed on the southern slopes, northern
103 slopes and interior (close to the ridge) of the Qilian Mountains, with three sites in the
104 eastern section [called Taola (TL), Huangchengshuiguan (HS) and Liuba (LB), from
105 south to north] and another three sites in the middle section [called Daladong (DLD),
106 Boligou (BLG) and Shandan (SD), from south to north]. The background of the Qilian
107 Mountains is shown on the satellite map in Figure 1a, and the six sites are marked on
108 the topographical map, also in Figure 1b. The distances between the six sites are listed
109 in Table 1. The sites in the south, north and interior are basically parallel to the
110 orientation of the mountains, and the sections formed by the sites in the east and interior
111 are basically perpendicular to it. On the basis of an historical weather review and rain
112 gauge observations, the rainy season at the six sites is concentrated in May to October,
113 with more precipitation in July, August and September.

114



115
 116 Figure 1. (a) Geographical overview of the Qian Mountains; (b) the disdrometer sites
 117 (circles); (c) the observation device at TL site. Source: Google Earth © Google Earth
 118 YEAR

119 Table 1. Site details (latitude, longitude, sea level height) and distances (km) between
 120 pairs of sites.

| Six sites | LB | HS | TL | SD | BLG | DLD |
|-------------------------------|----|------|------|-------|-------|-------|
| LB (38.16°N, 102.14°E, 1926m) | - | 39.6 | 94.3 | 116.0 | 129.6 | 161.1 |
| HS (37.83°N, 102.01°E, 2342m) | - | - | 55.6 | 135.1 | 132.8 | 154.9 |
| TL (37.33°N, 102.00°E, 2910m) | - | - | - | 182.4 | 167.3 | 177.0 |
| SD (38.80°N, 101.08°E, 1765m) | - | - | - | - | 54.2 | 96.8 |
| BLG (38.4°N, 100.69°E, 2455m) | - | - | - | - | - | 43.3 |
| DLD (38.18°N, 100.3°E, 2957m) | - | - | - | - | - | - |

121 This study used an optical, laser-based device to measure the DSD, called a DSG4
 122 disdrometer (Figure 1c), which meets the Functional Specification Requirements for
 123 Disdrometer issued by the China Meteorological Administration. This disdrometer has
 124 an HSC-OTT Parsivel2 sensor as the observation part, manufactured by OTT
 125 Messtechnik (Germany) and Huatron (China). When raindrops pass through the
 126 horizontal flat laser beam generated by the transmitting part of the instrument, it causes

127 signal attenuation in the laser observation area. The raindrop size is determined by the
 128 degree of signal attenuation and the falling speed is recorded by the transit time. The
 129 sampling time is 60s and the velocity and drop sizes are divided into 32 non-equally
 130 spaced bins, varying from 0.05 to 20.8 m s⁻¹ for velocity and 0.062 to 24.5 mm for drop
 131 diameter.

132 2.2 Quality control of the data

133 It was necessary to quality control the data because of potential instrument error.
 134 Every minute of DSD data collected by the six DSG4 disdrometers from May to
 135 October 2020 was carefully processed. Specifically, the following criteria were
 136 employed in choosing data for analysis(Jaffrain et al., 2011; Guyot et al., 2019; Pu et
 137 al., 2020): (1) the first two size bins were ignored because of low signal-to-noise ratio;
 138 (2) samples with 1-min total of raindrop number less than 10, or a rain rate at the
 139 moment of discontinuous observation less than 0.1 mmh⁻¹ were regarded as noise
 140 (corresponds to the second sample in Table 2); (3) raindrops with diameters more than
 141 8 mm were eliminated; (4) raindrops with a falling terminal velocity $V(D_i)$ that deviated
 142 from the empirical terminal velocity $V_{emp}(D_i)$ by more than 40% were removed (Kruger
 143 and Krajewski, 2002); and (5) samples with less than five bins after the correction of
 144 falling terminal velocity were deleted because their DSDs could not be determined with
 145 too few bins. The fourth criterion can be expressed by the formula:

$$146 \quad |V(D_i) - V_{emp}(D_i)| < 0.4V_{emp}(D_i) \quad (1)$$

147 where $V_{emp}(D_i) = 9.65 - 10.3\exp(-0.6D_i)$ (D_i is the mean volume-equivalent
 148 diameter of the i th size category), as derived from the formula given in Atlas et al.
 149 (1973).

150 After data quality control, the sample statistics of key steps are shown in Table 2.
 151 The number of 1-min DSD spectra selected from the six sites (LB, HS, TL, SD, BLG,
 152 DLD) after data quality control covering the rainy season (May–October) in the Qilian
 153 Mountains region in 2020 were 11103, 17619, 14814, 10736, 18861 and 13230,
 154 respectively, which accounted for 87.9%, 85.8%, 84.5%, 91.2%, 80.6% and 86.5% of
 155 the total number of samples.

156 Table 2. Sample statistics of data quality control at six sites

| Samples | LB | HS | TL | SD | BLG | DLD |
|--|-------|-------|-------|-------|-------|-------|
| Total minutes (min) | 12625 | 20536 | 17526 | 11770 | 23401 | 15289 |
| Total minutes without noise (min) | 12602 | 20509 | 17494 | 11756 | 23371 | 15267 |
| After quality control (min) | 11103 | 17619 | 14814 | 10736 | 18861 | 13230 |
| Available data-rain minutes (%) | 87.9% | 85.8% | 84.5% | 91.2% | 80.6% | 86.5% |

157

158 2.3 Integral parameters of rainfall

159 The basic observations obtained by the disdrometer were the counts of raindrops
 160 at each diameter and velocity. Also, the diameters given by the disdrometers were the
 161 mid value of two adjacent bins, which we take as the corresponding endpoint bin values.
 162 The velocities were the weighted average velocity class over the corresponding

163 disdrometer. The raindrop number concentration $N(D_i)$ ($\text{m}^{-3} \text{mm}^{-1}$) in the i th size bin
 164 per unit volume per unit size interval for diameter was calculated by the following
 165 equation:

$$166 \quad N(D_i) = \sum_{j=1}^{32} \frac{n_{i,j}}{A \cdot \Delta t \cdot V_j \cdot \Delta D_i} \quad (2)$$

167 where n_{ij} denotes the counts of raindrops measured by the disdrometer within size bin
 168 i and velocity bin j during the sampling time Δt ; A and Δt are the sampling area (0.0054
 169 m^2) and sampling time (60 s), respectively; V_j (m s^{-1}) is the mid-value falling speed for
 170 velocity bin j ; and ΔD_i is the diameter spread for the i th diameter bin.

171 Some integral rainfall parameters, such as the total number concentration N_t (m^{-3}),
 172 rain rate R (mm h^{-1}), radar reflectivity factor Z ($\text{mm}^6 \text{m}^{-3}$) and liquid water content W
 173 (g cm^{-3}), can be derived by the following equations:

$$174 \quad N_t = \sum_{i=1}^{32} N(D_i) \Delta D \quad (3)$$

$$175 \quad R = \frac{6\pi}{10^4 \rho_w} \sum_{i=1}^{32} V(D_i) D_i^3 N(D_i) \Delta D_j \quad (4)$$

$$176 \quad Z = \sum_{i=1}^{32} N(D_i) D_i^6 \Delta D_i \quad (5)$$

$$177 \quad W = \frac{\pi \rho_w}{6 \times 10^3} \sum_{i=1}^{32} D_i^3 N(D_i) \Delta D_i \quad (6)$$

178 where ρ_w is the water density (1.0 gcm^{-3}); and $V(D_i)$ is the falling speed from the
 179 disdrometer. In this study, when calculating the rain rate we use $V_{emp}(D_i)$ to replace $V(D_i)$
 180 because of measurement error, particularly at larger bins and faster falling speeds,
 181 [which is inspired from Tokay et al. \(2014\) and Zhang et al. \(2019\)](#).

182 The characteristics of DSD can be described by a three-parameter gamma
 183 distribution in the form introduced by Ulbrich (1983). Also, it has better fitting
 184 capability than the M-P distribution on the broader variation of DSD fluctuations,
 185 including the middle rain drops, especially on small and large rain scales. The three-
 186 parameter gamma distribution can be expressed by the following formula:

$$187 \quad N(D) = N_0 D^\mu \exp(-\Lambda D) \quad (7)$$

188 where $N(D)$ is the raindrop number concentration; D is the raindrop bins with unit mm ;
 189 and N_0 , μ and Λ are the intercept, shape and slope parameter from the three parameters
 190 of the gamma model, which can be derived from gamma moments or the least-squares
 191 method, respectively. When $\mu=0$, it degenerates into the M-P DSD model.

192 Although, the gamma distribution is commonly accepted, the normalized gamma
 193 distribution has also been widely adopted with its independent parameters and clear
 194 physical meaning as follows (Dolan et al., 2018; Ma et al., 2019):

$$195 \quad N(D) = \frac{3}{128} N_w \left[\frac{(4 + \mu)^{(4+\mu)}}{\Gamma(4 + \mu)} \right] \left(\frac{D}{D_m} \right)^\mu \exp\left(-\frac{(4 + \mu)D}{D_m} \right) \quad (8)$$

196 where μ is the shape parameter, which is in dimensionless; D_m (mm) is the mass-
 197 weighted mean diameter, and N_w ($\text{m}^{-3} \text{mm}^{-1}$) is the normalized intercept parameter
 198 computed from D_m . The form is as follows:

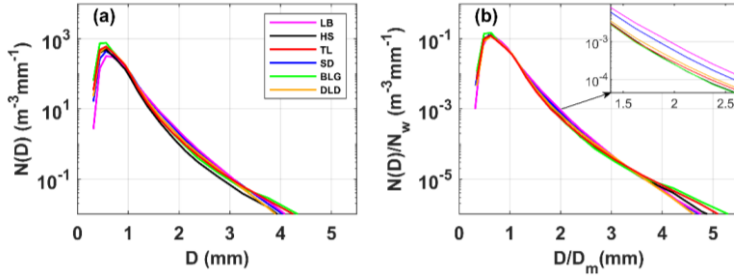
$$199 \quad D_m = \frac{\sum_{i=1}^{32} N(D_i) D_i^4 \Delta D_i}{\sum_{i=1}^{32} N(D_i) D_i^3 \Delta D_i} \quad (9)$$

$$200 \quad N_w = \frac{4^4}{\pi \rho_w} \left(\frac{10^3 W}{D_m^4} \right) \quad (10)$$

201 3 DSD parameter characteristics

202 3.1 Characteristics of DSD

203 Figure 2a shows the mean DSDs for the six sites during the rainy season in the
 204 Qilian Mountains. The maximum concentration of raindrops was around 0.562 mm in
 205 diameter and the maximum number concentration values of sites were order as follows:
 206 BLG>TL>DLD>HS>SD>LB. As the diameter increased, the number concentration
 207 decreased and the concentration values followed the order
 208 LB>SD>DLD>TL>BLG>HS at around 2 mm in diameter. When the diameter was
 209 larger than 4 mm, the concentration at TL, BLG and HS was relatively high. In this
 210 study, the data were roughly divided into small raindrops (less than 1 mm in diameter),
 211 midsize raindrops (1–3 mm) and large raindrops (greater than 3 mm) to easily describe
 212 the difference in DSDs (Ma et al., 2019b; Pu et al., 2020). To highlight the DSD
 213 differences caused by the background environment, Figure 2b shows the mean DSDs
 214 normalized by the N_w and D_m results for the sites. Compared with Figure 2a, the
 215 raindrop characteristics were more consistent across sizes, while the differences
 216 between the sites were more pronounced, especially in the midsize and large raindrops,
 217 which truly reflected the DSD differences caused by the location. Combining the
 218 characteristics of the geographical environment of the six sites, we can analyze some
 219 differences in DSD characteristics in the Qilian Mountains. For small raindrops, the
 220 number concentrations at interior and southern-slope sites were greater than at northern-
 221 slope sites; for midsize raindrops, the number concentrations decreased sequentially at
 222 the northern-slope, southern-slope and interior sites; and for large raindrops, the number
 223 concentrations at the interior sites were larger. In addition, the number concentrations
 224 of raindrops in the middle section of this the mountainous area were slightly greater
 225 than those in the eastern section.



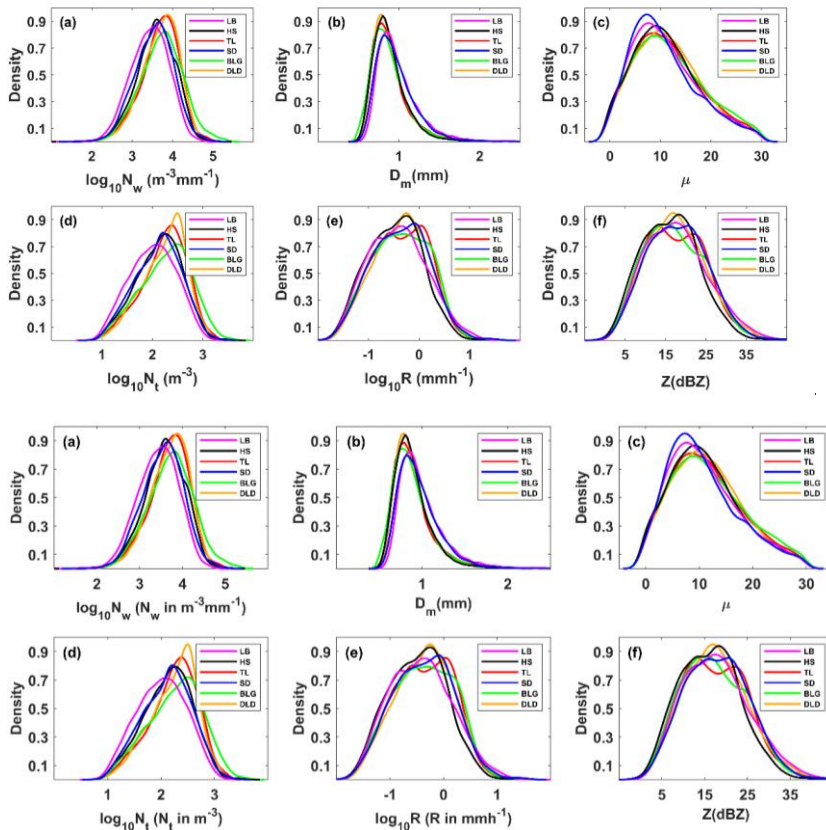
226

227 Figure 2. The (a) mean and (b) normalized mean DSDs at six sites in the Qilian
 228 Mountains region in the rainy season

229 **3.2 Distribution of DSD parameters**

230 In order to study the differences in DSDs, we selected six integral rainfall
 231 parameters for discussion—namely, the normalized intercept parameter (N_w), mass-
 232 weighted mean diameter (D_m), shape parameter (μ), total number concentration (N_t),
 233 rain rate (R) and radar reflectivity factor (Z). Figure 3 and Table 3 show the distributions
 234 and statistics of these six DSD parameters (the distribution of each was normalized
 235 using the uniform method). On average, D_m was more concentrated on smaller values
 236 at HS and BLG, which showed smaller mean values than TL and DLD but significantly
 237 more values greater than 1 mm at LB and SD; $\log_{10}N_w$ was more centralized on larger
 238 values at TL and DLD, with relatively smaller values at LB and SD; and the distribution
 239 patterns for μ and $\log_{10}N_t$ were similar to those for $\log_{10}N_w$. The density curves of R and
 240 Z were similar, but there were differences among the six sites, which are analyzed in
 241 detail later in the paper. It is noteworthy that the frequency of samples with R around
 242 $0.6\text{--}1.0\text{ mm h}^{-1}$ was highest, and samples with R less than 1 mm h^{-1} accounted for more
 243 than half of the total rainfall.

244



245

246 Figure 3. Probability density distribution of integral DSD parameters at six sites (LB,
 247 HS, TL, SD, BLG, DLD): (a) normalized intercept parameter $\log_{10}N_w$ (N_w in $m^{-3}mm^{-1}$);
 248 (b) mass-weighted mean diameter D_m (mm); (c) shape parameter μ ; (d) total number
 249 concentration $\log_{10}N_t$ (N_t in m^{-3}); (e) rain rate $\log_{10}R$ (R in $mm h^{-1}$); (f) radar reflectivity
 250 factor Z (dBZ)

251 Table 3. Statistical of several integral DSD parameters for all observations at six sites
 252 (LB, HS, TL, SD, BLG, DLD).

| Sites | $\log_{10}N_w$ ($m^{-3}mm^{-1}$) | | | D_m (mm) | | | μ | | | $\log_{10}N_t$ (m^{-3}) | | | R ($mm h^{-1}$) | | | Z (带格式的: 居中) | | |
|-------|------------------------------------|------|-------|------------|------|------|-------|------|------|-----------------------------|------|-------|---------------------|------|-------|----------------|------|------|
| | ME | SD | SK | ME | SD | SK | ME | SD | SK | ME | SD | SK | ME | SD | SK | ME | SD | SK |
| LB | 3.43 | 0.47 | -0.25 | 0.99 | 0.29 | 2.68 | 10.92 | 6.63 | 0.61 | 2.01 | 0.46 | -0.07 | 0.94 | 1.90 | 0.23 | 17.79 | 7.82 | 0.44 |
| HS | 3.59 | 0.48 | -0.29 | 0.89 | 0.25 | 3.35 | 11.12 | 6.64 | 0.53 | 2.13 | 0.45 | -0.22 | 0.69 | 1.60 | 0.05 | 16.24 | 7.08 | 0.34 |
| TL | 3.69 | 0.48 | -0.55 | 0.90 | 0.29 | 4.49 | 11.37 | 6.84 | 0.48 | 2.23 | 0.44 | -0.43 | 0.89 | 1.48 | -0.05 | 17.47 | 7.55 | 0.35 |
| SD | 3.54 | 0.48 | -0.17 | 0.96 | 0.26 | 2.12 | 10.62 | 6.61 | 0.71 | 2.11 | 0.46 | -0.17 | 0.97 | 2.01 | 0.06 | 17.95 | 7.47 | 0.28 |
| BLG | 3.72 | 0.54 | -0.15 | 0.89 | 0.29 | 5.17 | 11.71 | 7.06 | 0.46 | 2.26 | 0.50 | -0.25 | 0.94 | 2.13 | -0.04 | 17.34 | 7.66 | 0.41 |
| DLD | 3.69 | 0.45 | -0.50 | 0.90 | 0.25 | 2.66 | 11.52 | 6.66 | 0.43 | 2.24 | 0.43 | -0.46 | 0.95 | 1.62 | -0.01 | 17.70 | 7.43 | 0.37 |

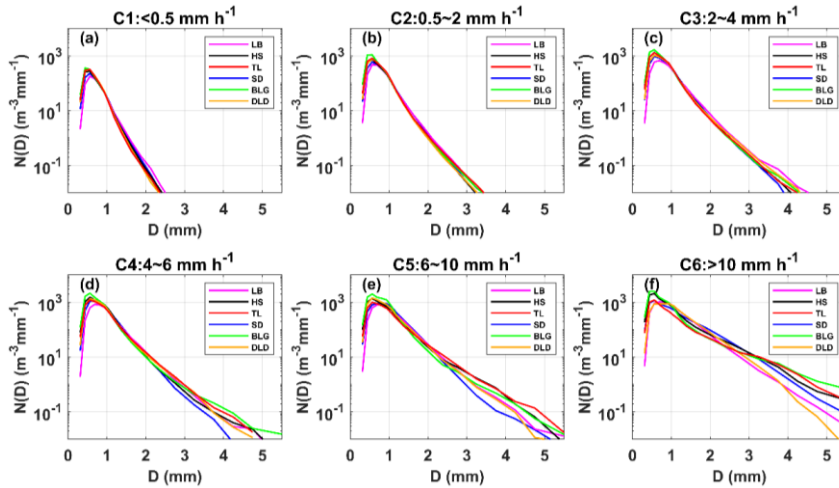
253 Note: ME is mean; SD is standard deviation; SK is skewness.

254 3.3 DSD characteristics in different rain rate classes

255 To further understand the characteristics of DSDs at the six sites, the samples were
 256 divided into six classes according to the associated rain rates (R): C1, $R < 0.5$; C2,
 257 $0.5 \leq R < 2$; C3, $2 \leq R < 4$; C4, $4 \leq R < 6$; C5, $6 \leq R < 10$; C6, $R \geq 10$ $mm h^{-1}$. This classification
 258 was based on two considerations: firstly, the number of observation samples in different
 259 rainfall rates roughly conformed to a normal distribution; and secondly, the mean
 260 maximum diameter interval of different rainfall rates gradually increased (Li et al.,
 261 2019). Of course, other classification studies were referenced and the fact that the rain
 262 rate in this area is smaller than that in southern China was taken into account (Ma et al.,
 263 2019b; Zeng et al., 2021). Figure 4 shows the mean DSDs at each rainfall rate class for
 264 the six sites. Table 4 lists the number of samples and statistical values of the DSD
 265 parameters for the six classes. Clearly, as the rainfall rate increased, the number
 266 concentration of almost all raindrop sizes and the width of DSD shapes increased, and
 267 thus the tail of the DSD shape moved gradually towards a larger diameter, similar to
 268 previous findings, such as those of Ma et al. (2019b) and Pu et al. (2020). Taking a
 269 number concentration of $0.01 m^{-3}mm^{-1}$, the mean maximum diameter of DSD in each
 270 class was ordered as follows: 2.3–2.5, 3.2–3.4, 3.9–4.5, 4.3–5.0, 5.0–5.6 and 6.0–7.0
 271 mm (the sixth-class diameter range is not fully shown in the figure). In class C1, the
 272 number concentrations were relatively similar at different sites; starting from class C2,
 273 the differences in number concentration increased when the diameter was greater than
 274 2 mm for the six sites; and the differences of in number concentration were gradually
 275 reflected in each raindrop size bin as the rainfall rate class increased. Observationally,
 276 the DSDs of BLG, HS and TL had larger number concentrations in different rainfall
 277 rate classes, and the DSD parameters and standard deviations (SDs) were larger,
 278 especially for BLG.

279 Table 4. Statistics of several integral DSD parameters for six rain rate classes at six sites.

| Class | Sites | Samples | $\log_{10}N_w$ | | D_m | | μ | | $\log_{10}N_r$ | | R | | Z | |
|-------------------------------|-------|---------|-------------------|------|--------|------|-------|------|----------------|------|----------------|------|-------|------|
| | | | $(m^{-3}mm^{-1})$ | | (mm) | | | | (m^{-3}) | | $(mm\ h^{-1})$ | | dBZ | |
| | | | ME | SD | ME | SD | ME | SD | ME | SD | ME | SD | ME | SD |
| C1(<0.5 mm h ⁻¹) | LB | 6520 | 3.25 | 0.41 | 0.88 | 0.18 | 12.36 | 7.09 | 1.74 | 0.34 | 0.20 | 0.13 | 12.68 | 4.52 |
| | HS | 10753 | 3.43 | 0.44 | 0.81 | 0.17 | 12.01 | 7.03 | 1.89 | 0.37 | 0.20 | 0.13 | 11.90 | 4.54 |
| | TL | 7858 | 3.52 | 0.44 | 0.79 | 0.16 | 12.91 | 7.12 | 1.96 | 0.37 | 0.20 | 0.13 | 11.78 | 4.16 |
| | SD | 5772 | 3.34 | 0.43 | 0.85 | 0.18 | 11.72 | 6.99 | 1.82 | 0.36 | 0.20 | 0.13 | 12.51 | 4.40 |
| | BLG | 10073 | 3.50 | 0.48 | 0.79 | 0.17 | 12.94 | 7.28 | 1.94 | 0.40 | 0.20 | 0.13 | 11.73 | 4.26 |
| | DLD | 6891 | 3.51 | 0.43 | 0.79 | 0.15 | 13.04 | 6.92 | 1.96 | 0.36 | 0.21 | 0.13 | 12.14 | 4.15 |
| C2(0.5~2 mm h ⁻¹) | LB | 3318 | 3.66 | 0.41 | 1.06 | 0.24 | 9.93 | 5.75 | 2.30 | 0.28 | 1.00 | 0.41 | 22.55 | 3.27 |
| | HS | 5700 | 3.82 | 0.39 | 0.97 | 0.21 | 10.21 | 5.88 | 2.44 | 0.26 | 0.96 | 0.37 | 21.67 | 3.09 |
| | TL | 5368 | 3.87 | 0.42 | 0.98 | 0.23 | 10.35 | 6.15 | 2.49 | 0.26 | 1.07 | 0.41 | 22.18 | 3.33 |
| | SD | 3778 | 3.73 | 0.41 | 1.03 | 0.23 | 9.94 | 6.14 | 2.36 | 0.28 | 1.02 | 0.40 | 22.40 | 3.15 |
| | BLG | 6411 | 3.97 | 0.47 | 0.94 | 0.25 | 11.24 | 6.72 | 2.56 | 0.30 | 1.07 | 0.43 | 21.69 | 3.69 |
| | DLD | 4778 | 3.88 | 0.37 | 0.95 | 0.20 | 10.91 | 6.02 | 2.47 | 0.24 | 1.01 | 0.40 | 21.60 | 3.19 |
| C3(2~4 mm h ⁻¹) | LB | 782 | 3.71 | 0.47 | 1.31 | 0.37 | 7.33 | 4.28 | 2.52 | 0.29 | 2.77 | 0.56 | 29.54 | 2.87 |
| | HS | 884 | 3.96 | 0.50 | 1.16 | 0.34 | 8.42 | 5.22 | 2.73 | 0.27 | 2.76 | 0.54 | 28.33 | 3.06 |
| | TL | 1232 | 4.00 | 0.47 | 1.13 | 0.33 | 8.70 | 5.93 | 2.75 | 0.23 | 2.68 | 0.53 | 28.07 | 3.16 |
| | SD | 812 | 3.89 | 0.44 | 1.19 | 0.27 | 8.57 | 5.53 | 2.63 | 0.26 | 2.71 | 0.53 | 28.41 | 2.68 |
| | BLG | 1865 | 4.05 | 0.49 | 1.11 | 0.30 | 8.62 | 5.75 | 2.81 | 0.25 | 2.70 | 0.53 | 27.99 | 3.29 |
| | DLD | 1111 | 3.91 | 0.44 | 1.18 | 0.29 | 7.81 | 5.45 | 2.70 | 0.23 | 2.74 | 0.54 | 28.73 | 3.09 |
| C4(4~6 mm h ⁻¹) | LB | 229 | 3.80 | 0.47 | 1.41 | 0.40 | 7.33 | 3.94 | 2.65 | 0.31 | 4.76 | 0.57 | 32.69 | 2.63 |
| | HS | 191 | 4.03 | 0.54 | 1.28 | 0.47 | 7.54 | 4.42 | 2.86 | 0.27 | 4.80 | 0.56 | 31.70 | 3.34 |
| | TL | 213 | 3.84 | 0.56 | 1.41 | 0.51 | 6.23 | 4.64 | 2.77 | 0.28 | 4.77 | 0.54 | 32.82 | 3.54 |
| | SD | 187 | 4.03 | 0.41 | 1.24 | 0.27 | 8.35 | 5.02 | 2.80 | 0.22 | 4.76 | 0.54 | 31.32 | 2.52 |
| | BLG | 321 | 3.99 | 0.66 | 1.33 | 0.53 | 7.97 | 6.10 | 2.93 | 0.27 | 4.78 | 0.54 | 32.44 | 4.40 |
| | DLD | 270 | 3.92 | 0.53 | 1.35 | 0.47 | 6.50 | 4.80 | 2.83 | 0.25 | 4.83 | 0.56 | 32.55 | 3.47 |
| C5(6~10 mm h ⁻¹) | LB | 167 | 3.81 | 0.46 | 1.55 | 0.44 | 6.46 | 3.38 | 2.72 | 0.27 | 7.66 | 1.22 | 35.74 | 2.85 |
| | HS | 49 | 3.69 | 0.74 | 1.70 | 0.68 | 6.89 | 4.82 | 2.75 | 0.38 | 7.42 | 1.09 | 36.14 | 4.29 |
| | TL | 103 | 3.57 | 0.62 | 1.78 | 0.66 | 5.20 | 4.62 | 2.71 | 0.32 | 7.32 | 1.02 | 37.03 | 3.76 |
| | SD | 128 | 3.96 | 0.39 | 1.42 | 0.35 | 7.10 | 3.96 | 2.82 | 0.21 | 7.68 | 1.17 | 34.76 | 2.42 |
| | BLG | 138 | 3.97 | 0.76 | 1.51 | 0.80 | 8.34 | 6.35 | 2.99 | 0.27 | 7.37 | 1.02 | 35.09 | 4.96 |
| | DLD | 122 | 3.90 | 0.46 | 1.46 | 0.34 | 6.13 | 4.20 | 2.86 | 0.26 | 7.29 | 1.11 | 35.32 | 2.88 |
| C6(>10 mm h ⁻¹) | LB | 87 | 3.85 | 0.44 | 1.73 | 0.53 | 5.08 | 3.05 | 2.87 | 0.32 | 14.81 | 7.57 | 39.58 | 3.57 |
| | HS | 42 | 3.60 | 0.65 | 2.19 | 0.92 | 6.74 | 5.27 | 3.00 | 0.28 | 21.69 | 9.91 | 42.93 | 6.11 |
| | TL | 40 | 3.16 | 0.69 | 2.69 | 1.19 | 4.34 | 5.20 | 2.74 | 0.32 | 18.25 | 9.69 | 44.70 | 5.41 |
| | SD | 59 | 3.66 | 0.29 | 2.04 | 0.46 | 3.30 | 2.48 | 2.91 | 0.16 | 21.07 | 8.34 | 42.85 | 4.10 |
| | BLG | 53 | 3.38 | 0.93 | 2.58 | 1.52 | 5.58 | 6.19 | 3.00 | 0.37 | 21.95 | 9.05 | 44.08 | 7.50 |
| | DLD | 58 | 3.82 | 0.47 | 1.80 | 0.46 | 6.64 | 4.12 | 2.84 | 0.28 | 16.58 | 7.21 | 40.13 | 3.53 |



280

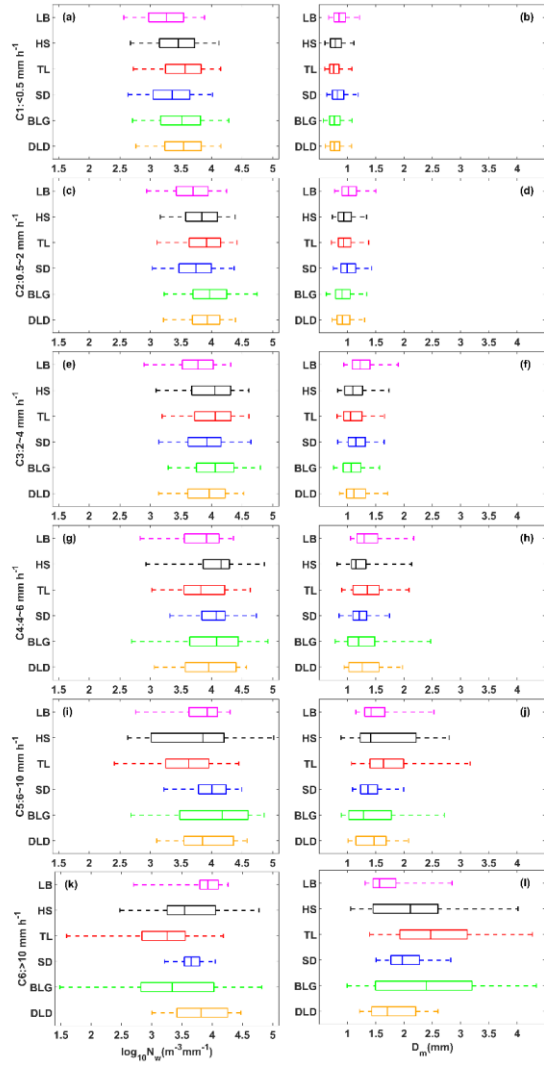
281 Figure 4. Distribution of mean measured DSD for different rain rate classes at six sites.

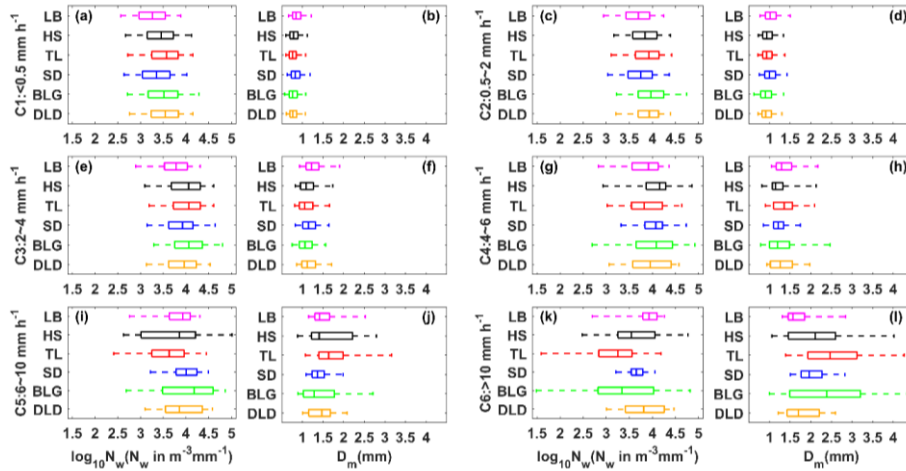
282 Figure 5 shows box-and-whisker plots of the normalized intercept parameter
 283 $\log_{10}N_w$ and mass-weighted mean diameter D_m for six sites in each rain rate class. The
 284 middle line in the box indicates the median. The left and right lines indicate the 25th and
 285 75th percentiles. The left and right ends of whiskers indicate the most extreme data
 286 points between the 5th and 95th percentiles, except outliers. The median D_m gradually
 287 increased with a larger value range as the rain rate class increased, particularly for HS
 288 and BLG in class C5 and C6. The median $\log_{10}N_w$ increased in class C1 to C3 and then
 289 tended to decrease in class C5 to C6, for which the reduction was obvious at sites with
 290 a larger value range, such as HS and BLG. Ma et al. (2019b) also obtained similar
 291 conclusions about D_m and $\log_{10}N_w$ that D_m values increase with the increased rainfall
 292 intensity, while the $\log_{10}N_w$ is not as clear. The indication was that the increase in rain
 293 rate was mainly due to the growth in raindrop size. Also, the change in number
 294 concentration may have been caused by the imbalance between the loss of number
 295 concentration at small raindrop size and the addition at large raindrop sizes, which in a
 296 sense implies a relationship between the collision-coalescence and break-up of
 297 raindrops. It is worth noting that the microphysical processes were quite different
 298 among the sites, being greatly influenced by the surrounding environment. Because HS
 299 and BLG were located in the interior of the mountains and close to the ridge, their
 300 dynamics and thermodynamics as well underlying surfaces were thus different from
 301 those of other sites.

带格式的：下标

带格式的：下标

带格式的：下标

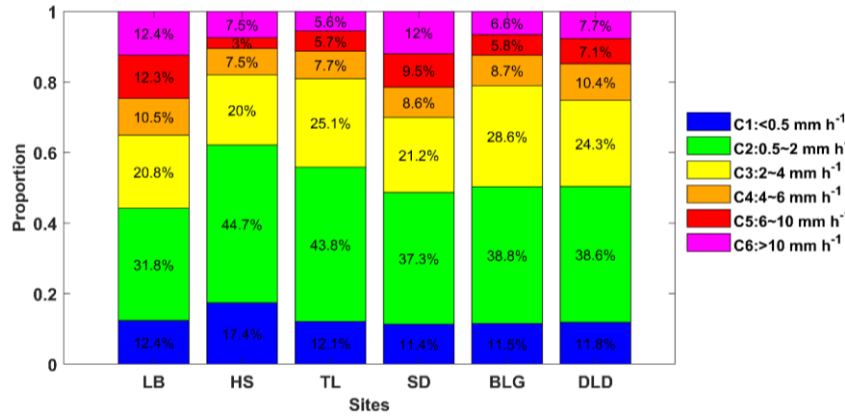




303

304 Figure 5. Variation of the normalized intercept parameter $\log_{10}N_w$ (a) and the mass-
 305 weighted mean diameter D_m (b) for different rain rate classes at six sites. The three lines
 306 in the boxes are the 25th, 50th and 75th percentiles, from left to right, respectively. The
 307 whiskers at the left and right ends are the 5th and 95th percentiles, respectively. The
 308 colors represent the six sites as in other figures.

309 Figure 6 displays the contribution of different rain rate classes to the total rainfall
 310 at different sites. It is clear that C2 contributed the most to the total rainfall of all sites,
 311 followed by C3, and the sum of the two classes' contribution could reach 60% of the
 312 total rainfall. Compared with the interior and southern-slope sites, C2 and C3
 313 contributed slightly less to sites LB and SD (i.e., the northern slopes), while C5 and C6
 314 contributed relatively more to sites LB and SD, indicating that there is a greater
 315 probability of heavy precipitation events on the northern slopes. The DSD parameters
 316 in Table 3 provide a more detailed representation of the rainfall differences between the
 317 three geographical sections of the Qilian Mountains, i.e., the interior, southern slopes
 318 and northern slopes. Meanwhile, it also reflects the characteristics of rainfall in the
 319 eastern and interior sections, such as the eastern section had larger Z and D_m and smaller
 320 $\log_{10}N_w$ and $\log_{10}N_t$ compared to the interior. It is possible that there is a certain spatial
 321 connection between precipitation at the sites, related to factors such as the source of
 322 precipitation vapor, weather system and so on.



323

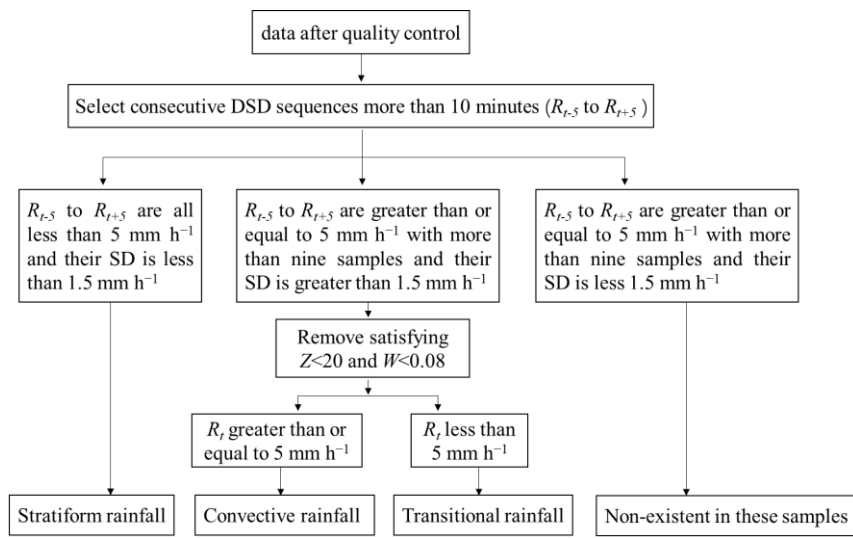
324 Figure 6. Proportion of rainfall with different rain rate classes to rain amount at six sites.

325 3.4 DSD properties for different rain types

326 Previous studies on DSD have shown that there are significant differences in the
 327 DSD of convective and stratiform rainfall in the same climatic region, which has a
 328 substantial impact on the parameterization of NWP and remote sensing observations
 329 (Bringi et al., 2003; Penide et al., 2013). Due to the different physical mechanisms of
 330 convective and stratiform rainfall, it is possible to discuss the differences in
 331 microphysical structures for rainfall types through their DSD. Studies have employed
 332 many different classification methods for rainfall types; example, Testud et al. (2001)
 333 used the rain rate; Chen et al. (2013) combined the rain rate and its SD; and the findings
 334 of Das et al. (2018) were based on the rain rate and radar reflectivity factor. Among
 335 these, the method of Chen et al. (2013) has commonly been used to establish samples
 336 of convective and stratiform rainfall, but mainly in semi-humid or humid regions with
 337 relatively high rain rate and rainfall. However, the Qilian Mountains are located in the
 338 semi-arid regions of China and far from the sea, where the average rainfall rain and
 339 rainfall are quite different from in semi-humid regions. Therefore, this paper proposes
 340 a new classification method for precipitation applicable to the arid and semi-arid
 341 regions of Northwest China based on the classification ideas of Chen et al. (2013) and
 342 Das et al. (2018).

343 Firstly, the sequences of DSD with continuous 1-min samples more than 10 min
 344 are determined, and R_t is defined as the rain rate at time t . In the first case, the R of
 345 samples from R_{t-5} to R_{t+5} are all less than 5 mm h^{-1} and their SD is less than 1.5 mm
 346 h^{-1} ; in the second case, the R of samples from R_{t-5} to R_{t+5} are greater than or equal to 5
 347 mm h^{-1} with more than nine samples and their SD is greater than 1.5 mm h^{-1} ; and in
 348 the third case, the situation is the same as the second case but their SD is less 1.5 mm
 349 h^{-1} . Secondly, samples satisfying $Z < 20$ and $W < 0.08$ in the second case are removed
 350 (Thurai et al., 2016; Das et al., 2018). And then, samples with R_t greater than or equal
 351 to 5 mm h^{-1} in the second case are regarded as convective rainfall and samples with R_t
 352 less than 5 mm h^{-1} in the second case are regarded as transitional rainfall (the rainfall

353 stage in which convective precipitation develops and declines). Samples in the first case
 354 are regarded as stratiform rainfall. Through experiments, the third case does not exist.
 355 The main calculation process is shown in Figure 7



356

357 Figure 7. Classification method for rainfall types in the Qilian Mountains.

带格式的: 居中, 缩进: 首行缩进: 0 字符, 段落间距
段前: 0.5 行, 段后: 0.5 行

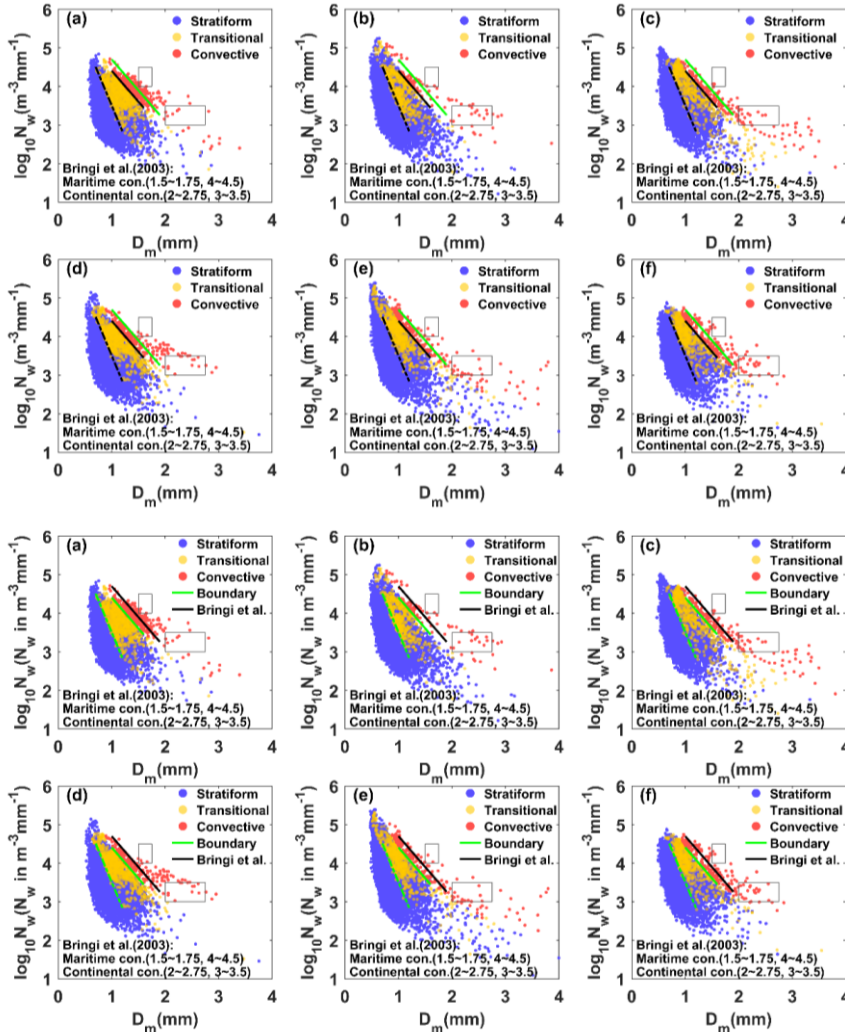
358 The $\log_{10}N_w$ and D_m of different rainfall types were different, which were taken as
 359 the main research objects. Figure 7.8 shows the variation of $\log_{10}N_w$ with D_m at different
 360 sites. The blue, red and yellow scatter points represent stratiform, convective and
 361 transitional rainfall, respectively. Obviously, there are fairly clear boundaries between
 362 the scatter points for the different precipitation type events, and the same dividing line
 363 can be used to distinguish between the different rainfall types at different sites. The
 364 ~~green~~ solid lines were drawn based on visual examination of the data with a slope
 365 of approximately -1.60 and intercept of 6.008 to represent the split between stratiform,
 366 transitional and convective rainfall in all subplots. The ~~black-green~~ dashed line can
 367 distinguish transitional rainfall (transitional and stratiform rainfall have an overlap area)
 368 with a slope of approximately -3.338 and intercept of 6.847 . Note that the dividing line
 369 between stratiform and convective rainfall has the same slope as that obtained by Bringi
 370 et al. (2003) (solid green line with a slope of -1.6 and intercept of 6.3), who fitted
 371 composite results based on disdrometer data and from radar retrievals covering many
 372 climate conditions from near the equator to plateau. The $\log_{10}N_w$ and D_m from the
 373 figures for stratiform, convective and transitional rainfall are respectively concentrated
 374 in the ranges of $3.1-3.9\text{-m}^{-3}\text{mm}^{-1}$, $0.75-1.1\text{ mm}$; $3.8-4.2\text{-m}^{-3}\text{mm}^{-1}$, $1.4-1.6\text{ mm}$; $3.6-$
 375 $4.0\text{-m}^{-3}\text{mm}^{-1}$, $1.05-1.2\text{ mm}$. Compared to the maritime-like cluster and continental-like
 376 cluster of convective rainfall proposed by Bringi et al. (2003), the convective events in
 377 the Qilian Mountains are not belong to more consistent with the continental-like cluster
 378 or maritime-like cluster (the gray rectangle with smaller $\log_{10}N_w$ and larger D_m in Fig.
 379 7), while the averages of D_m are slightly less than the continental-like cluster and the

带格式的: 字体: 倾斜

带格式的: 字体: 倾斜, 下标

带格式的: 字体: 非倾斜

380 averages of $\log_{10}N_w$ are greater than the continental-like cluster. There are isolated
381 convective events in the maritime-like cluster, but it is difficult to have more events
382 from the trend between $\log_{10}N_w$ and D_m . This is also consistent with the features of the
383 geographical location of the Qilian Mountains.



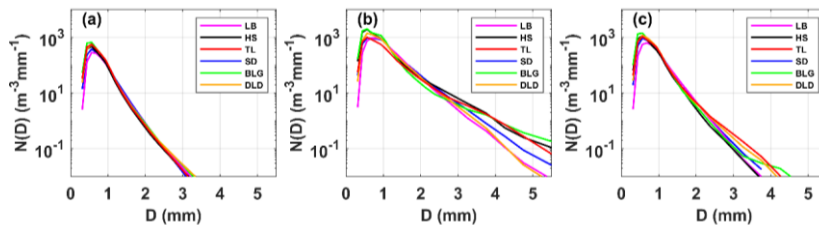
384

385

386 Figure 87. Scatter plot of $\log_{10}N_w$ versus D_m for different rain types at (a) LB, (b) HS,
387 (c) TL, (d)SD, (e)BLG, and (f)DLD. The stratiform cases, convective cases and
388 transitional cases are represented by blue, red and yellow scatter points, respectively.
389 The black-green dashed lines are the $\log_{10}N_w$ - D_m relationship for stratiform versus
390 convective cases and stratiform versus transitional case. The black dashed lines are the
391 $\log_{10}N_w$ - D_m relationship for stratiform versus convective cases and stratiform versus
392 transitional case from Bringi et al. (2003). The green dotted lines are the area of overlap

393 [between stratiform and transitional case.](#)

394 Figure 8-9 shows the mean DSDs for stratiform, convective and transitional
395 rainfall at the six sites. The range of number concentrations and corresponding raindrop
396 diameters for the three types were significantly different, matching the basic
397 characteristics of DSD. The mean DSDs of stratiform rainfall differed slightly among
398 the sites; convective rainfall had big differences at among the sites; and transitional
399 rainfall presented more differences beginning at larger than 2.2 mm in diameter, which
400 were the expected results. Stratiform rainfall usually has a large horizontal extent and
401 an homogeneous cloud distribution, which makes the DSD characteristics basically the
402 same under the influence of the same cloud system in mountainous areas. However,
403 convective rainfall is related to local thermal and dynamical factors, which could lead
404 to differences in DSD at different sites when considering the complex topography and
405 diverse underlying surfaces in mountainous areas. For example, for convective rainfall,
406 there was a significant increase in the number concentration of raindrops larger than 2.2
407 mm in diameter at BLG, HS and TL, indicating that these sites are conducive to the
408 development of convective precipitation. Also, the number concentration of small
409 raindrops at BLG and HS were higher than at TL (the southern slope), which may be
410 due to the higher altitude of the interior sites reducing the falling distance of raindrops
411 after exiting the cloud and decreasing the impact of collision on the raindrop evolution.
412 In other words, even for the same rainfall type, the microphysics of rainfall at different
413 sites is still different, depending on the topography and position of the observation point
414 relative to the cloud base.



415
416 Figure 98. Distribution of mean measured DSD for (a) stratiform rainfall, (b) convective
417 rainfall and (c) transitional rainfall at six sites.

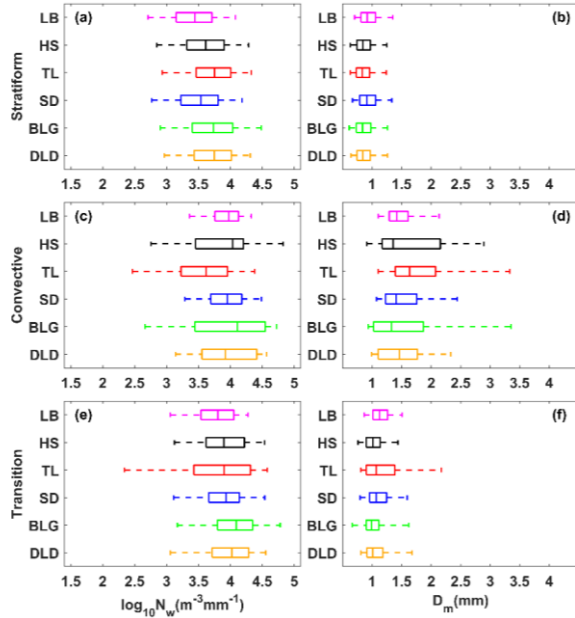
418 Figure 9-10 shows box-and-whisker plots of $\log_{10}N_w$ and D_m for different rain types.
419 The $\log_{10}N_w$ and D_m of stratiform rainfall were smaller than those of convective rainfall
420 but larger than those of transitional rainfall. Sites with a large $\log_{10}N_w$ value range had
421 larger value ranges for D_m ; and sites with a large median $\log_{10}N_w$ had a smaller median
422 D_m , especially at sites HS and BLG for convective rainfall. Based on the mean values
423 of the six sites in Table 5, the DSD characteristics in the Qilian Mountains consist of a
424 larger N_w and smaller D_m ([compared the results of studies in other regions, seeing](#)
425 [discussion section for details](#)) due to the melting of tiny, compact graupel, and rimed
426 ice particles (relative to large, low-density snowflakes). Compared with transitional
427 rainfall, the D_m of convective rainfall was obviously larger, indicating that the increase
428 in rain rate in this area is mainly due to the growth in raindrop size. Moreover, on the

429 northern slopes one should consider the increase in number concentration, because the
 430 $\log_{10}N_w$ of convective rainfall also increased. Note that the number of convective
 431 samples on the northern slopes was higher than that of other sites, which corresponds
 432 to the speculation regarding the contribution of different rain rate classes. On average,
 433 for stratiform rainfall, the dispersion degree of $\log_{10}N_w$ and D_m at different sites was
 434 8.3% and 10.0%, respectively; and for convective rainfall it was 10.4% and 23.4%. The
 435 SDs of DSD parameters at sites HS and BLG were relatively large.

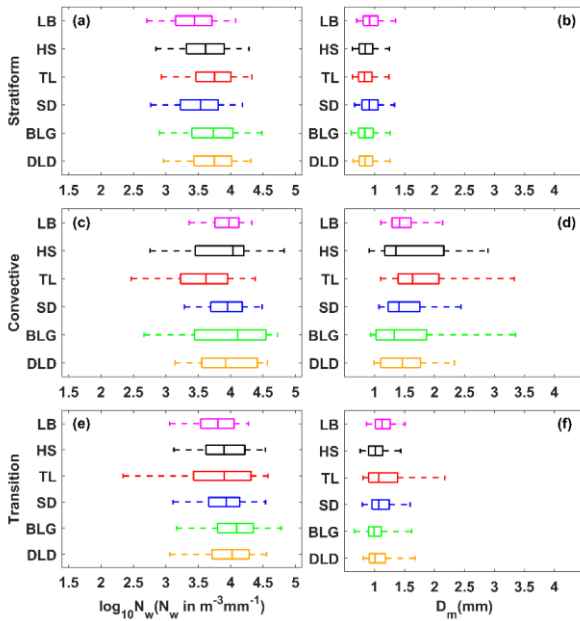
436 Table 5 Statistics of several integral DSD parameters for six sites with stratiform rainfall,
 437 convective rainfall and transitional rainfall

| Type | Sites | No. samples | $\log_{10}N_w$ | | D_m | | μ | | $\log_{10}N_t$ | | R | | Z | |
|------|-------|-------------|---|------|-----------------|------|-------|------|----------------------------------|------|--------------------------------------|-------|----------------|------|
| | | | ($m^{-3}mm^{-1}$) | | (mm) | | | | (m^{-3}) | | ($mm\ h^{-1}$) | | dBZ | |
| | | | ME | SD | ME | SD | ME | SD | ME | SD | ME | SD | ME | SD |
| S | LB | 7123 | 3.42 | 0.42 | 0.96 | 0.21 | 11.48 | 7.98 | 1.98 | 0.38 | 0.54 | 0.60 | 16.93 | 5.93 |
| | HS | 12694 | 3.60 | 0.44 | 0.88 | 0.21 | 11.24 | 7.89 | 2.14 | 0.40 | 0.54 | 0.58 | 16.17 | 6.06 |
| | TL | 10091 | 3.71 | 0.43 | 0.87 | 0.20 | 11.90 | 8.01 | 2.23 | 0.39 | 0.65 | 0.67 | 16.85 | 6.15 |
| | SD | 7175 | 3.51 | 0.44 | 0.95 | 0.22 | 11.15 | 8.03 | 2.07 | 0.39 | 0.62 | 0.64 | 17.36 | 6.10 |
| | BLG | 12467 | 3.72 | 0.49 | 0.88 | 0.23 | 12.24 | 8.50 | 2.25 | 0.44 | 0.70 | 0.74 | 17.11 | 6.33 |
| | DLD | 9685 | 3.70 | 0.42 | 0.88 | 0.21 | 11.91 | 7.91 | 2.23 | 0.38 | 0.67 | 0.69 | 17.18 | 6.13 |
| C | LB | 292 | 3.91 | 0.35 | 1.49 | 0.35 | 6.50 | 3.30 | 2.81 | 0.23 | 9.28 | 5.56 | 35.88 | 3.59 |
| | HS | 100 | 3.85 | 0.67 | 1.71 | 0.84 | 6.33 | 4.33 | 2.95 | 0.30 | 12.55 | 13.75 | 37.32 | 6.64 |
| | TL | 159 | 3.54 | 0.59 | 1.87 | 0.74 | 5.21 | 4.97 | 2.72 | 0.30 | 9.48 | 6.91 | 37.96 | 5.21 |
| | SD | 219 | 3.91 | 0.37 | 1.54 | 0.47 | 6.61 | 4.68 | 2.85 | 0.19 | 10.75 | 7.68 | 36.24 | 5.02 |
| | BLG | 198 | 3.91 | 0.74 | 1.64 | 0.97 | 8.00 | 7.37 | 3.00 | 0.27 | 10.57 | 15.49 | 36.29 | 6.75 |
| | DLD | 203 | 3.94 | 0.48 | 1.50 | 0.43 | 6.96 | 5.24 | 2.87 | 0.27 | 9.41 | 6.04 | 35.89 | 4.27 |
| T | LB | 787 | 3.76 | 0.39 | 1.15 | 0.21 | 8.37 | 4.35 | 2.47 | 0.31 | 2.16 | 1.25 | 26.42 | 3.89 |
| | HS | 541 | 3.89 | 0.49 | 1.05 | 0.29 | 8.98 | 6.74 | 2.59 | 0.33 | 1.81 | 1.15 | 24.79 | 3.89 |
| | TL | 465 | 3.77 | 0.70 | 1.22 | 0.49 | 8.81 | 6.91 | 2.56 | 0.44 | 2.30 | 1.21 | 27.10 | 4.39 |
| | SD | 819 | 3.87 | 0.41 | 1.12 | 0.26 | 8.23 | 5.46 | 2.59 | 0.28 | 2.28 | 1.18 | 26.59 | 4.04 |
| | BLG | 665 | 4.04 | 0.51 | 1.04 | 0.31 | 10.33 | 7.31 | 2.72 | 0.33 | 2.19 | 1.13 | 25.66 | 4.44 |
| | DLD | 503 | 3.95 | 0.46 | 1.10 | 0.30 | 8.69 | 6.16 | 2.67 | 0.31 | 2.35 | 1.17 | 26.60 | 4.20 |

438



439



440

Figure 9¹⁰. As in Fig. 5 but for different rain types at six sites.

441

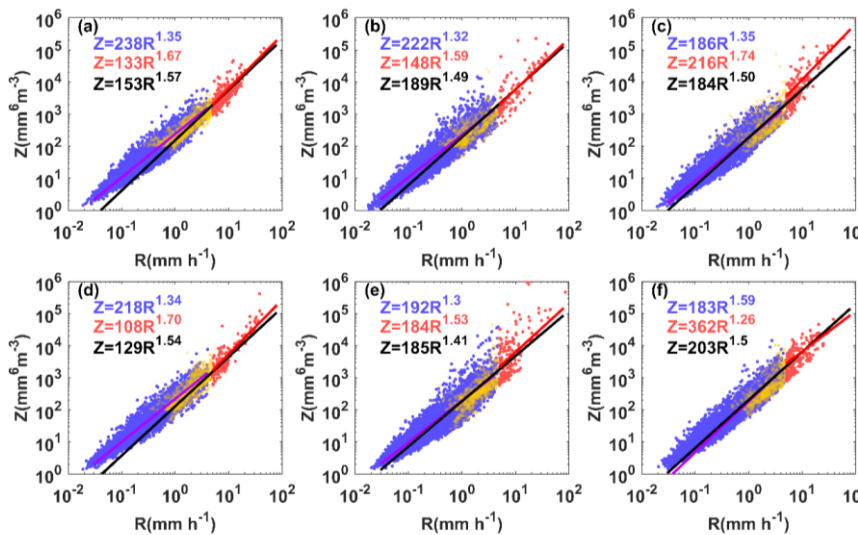
3.5 Implications for radar rainfall estimation with DSD

442

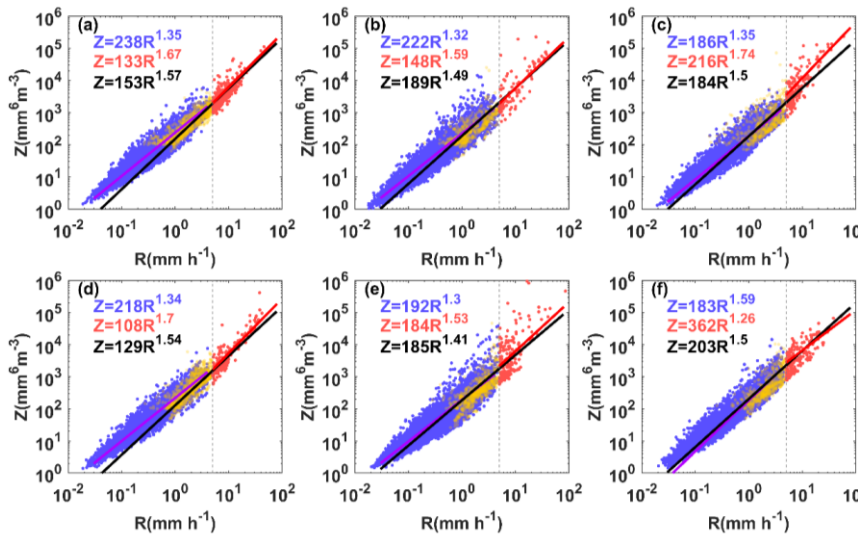
The sixth moment of raindrop diameter is proportional to the radar reflectivity

443 factor and the 3.76th moment is approximately the rain rate (they can be calculated by
 444 Equations 4 and 5). Generally, the theoretical basis of QPE for single polarization radar
 445 (ground-based or space-based) is the power relationship between the radar reflectivity
 446 and rainfall rate ($Z=AR^b$). This makes the coefficients A and exponents b of the power
 447 relationship heavily dependent on the variation in DSD. Therefore, it is necessary to
 448 obtain the A and b of different sites according to different rainfall types.

449 Figure 10-11 shows the Z - R scatter plots for different sites and the fitted power-
 450 law relationships for different rainfall types. The blue and red scatter points represent
 451 stratiform and convective rainfall, respectively. The purple, red and black solid lines
 452 indicate the Z - R relationships for stratiform, convective and total rainfall, respectively.
 453 It shows that the Z - R scatter points for HS and BLG were relatively scattered around
 454 the 5 mm h^{-1} rain rate. Besides, the Z - R relationship of total rainfall underestimated the
 455 stratiform rainfall at low R values and the convective rainfall at high R values. Based
 456 on the average Z - R relationship using a least-squares method, the dispersion degree of
 457 A and b at different sites was 42.5% and 10.7%, respectively, which reveals there to be
 458 large differences in mountain areas.



459



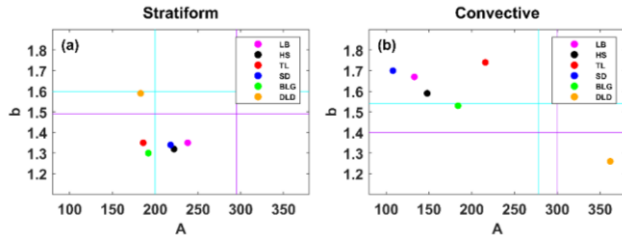
带格式的：居中

460

461 Figure 10.11. Scatter plots of Z ($\text{mm}^6 \text{m}^{-3}$) versus R (mm h^{-1}) for three rain types at (a)
 462 LB, (b) HS, (c) TL, (d)SD, (e)BLG, and (f)DLD. The blue, red and yellow scatter points,
 463 represent stratiform, convective and transitional cases, respectively. The purple, red and
 464 black lines denote the Z - R relationships. The blue, red and black formula denote stratiform,
 465 convective and total Z - R relationships. The grey dashed line indicates r is 5 mmh^{-1}

带格式的：上标

466 In order to compare the six sites Z - R relationships with some standard Z - R
 467 relationships, the results for $Z=300R^{1.4}$ for convective rainfall commonly used in radar,
 468 and $Z=200R^{1.6}$ (i.e., M48) for stratiform rainfall commonly used in midlatitude areas,
 469 are provided in Figure 10.12. Overall, convective rainfall had smaller values of A and
 470 larger values of b than those of stratiform rainfall (excluding DLD). The A values of
 471 convective rainfall were smaller than the commonly used Z - R relationship with large
 472 differences, but the b values were greater. The distribution of A and b for stratiform
 473 rainfall was relatively concentrated, with A and b ranging from 186–238 and 1.3–1.35,
 474 respectively. The A values of stratiform rainfallSR were close to those of M48, and the
 475 b values were close to and smaller than the Z - R of global stratiform rainfallSR.
 476 StationSite DLD had a similar Z - R for stratiform rainfall with as M48, while its
 477 convective rainfall was different from other sites, with a larger A value (twice as large
 478 as other sites) and smaller b value, which probably relates to its own local climatic
 479 influences formed in a narrow valley. In addition, it is clear that the A value of stratiform
 480 rainfall increased from the southern slopes to northern slopes, while the opposite was
 481 the case for convective rainfall. Also, the Z - R relationships of the same section are more
 482 consistent, such as those of the interior or the northern slopes, which have distinct
 483 geographic characteristics.



484
 485 Figure 4. The A and b values of the Z - R relationships for (a) stratiform rainfall and
 486 (b) convective rainfall at six sites. The purple lines in (a) and cyan lines in (b)
 487 correspond to the global Z - R model ($Z = 295R^{1.49}$ for continental stratiform rainfall and
 488 $Z = 278R^{1.54}$ for convective rainfall, respectively) (Ghada et al., 2018). The cyan lines
 489 in (a) represent the midlatitude stratiform rainfall Z - R model ($Z = 200R^{1.60}$, Marshall,
 490 1948); and the purple lines in (b) represent the convective rainfall Z - R model ($Z =$
 491 $300R^{1.40}$) applied to operational weather radar (Fulton et al., 1998).

492 **4 Discussion**

493 The paper analyses the statistical characteristics of DSD at different sites in the
 494 Qilian Mountains during the rainy season, which not only contain rainfall classes and
 495 rainfall types but more importantly reflect the differences between different sites. The
 496 results from different aspects can be mutually confirmed and have a good representation
 497 of the spatial distribution, serving as a strong factual basis for discussion of the
 498 microphysical structure of precipitation. For example, with the rain rate class rising, the
 499 number concentration of all size bins is increased and the width of DSDs became wider,
 500 which manifested as convective rainfall having a larger rain rate. In spatial terms, the
 501 characteristics of precipitation in the interior of the mountains and on the southern
 502 slopes were closer, whether considering the overall DSD distribution or the
 503 distributions of DSD parameters. However, there were obvious variabilities at the
 504 interior sites for DSD parameters due to the influences of local dynamics and thermal
 505 effects. On the other hand, these characteristics also exhibited some differences between
 506 the interior and eastern sections of the Qilian Mountains, especially in the discussion of
 507 DSD parameters for rainfall classes and rainfall types (s Figures 5 and 9.10). This spatial
 508 variation in DSD suggests that microphysical processes involved in the DSD are
 509 influenced by complex topography (altitude, mountain alignment) and potentially
 510 related to the source of water vapor, development of precipitation process and
 511 anthropogenic factors.

512 Compared to previous studies that focused on eastern [3.48 for $\log_{10}N_w$ and 1.23
 513 mm for D_m , Pu et al.(2020)], southern [3.86 for $\log_{10}N_w$ and 1.47 mm for D_m , Zhang et
 514 al.(2019)], and northern [3.60 for $\log_{10}N_w$ and 1.15 mm for D_m , Ma et al.(2019b)] and
 515 central [3.48 for $\log_{10}N_w$ and 1.54 mm for D_m , Fu et al.(2020)] China as well the Tibetan
 516 Plateau [3.47 for $\log_{10}N_w$ and 1.05 mm for D_m , Wang et al.(2021)], the Qilian Mountains
 517 region has its own unique DSD characteristics and Z - R relationship during the rainy
 518 season, including a smaller raindrop diameter with a higher number concentration [3.69
 519 for $\log_{10}N_w$ and 0.94 mm for D_m]. Moreover, the division of rainfall rate classes in the

- 带格式的: 字体: 倾斜
- 带格式的: 字体: 倾斜, 下标
- 带格式的: 字体: 倾斜
- 带格式的: 字体: 倾斜
- 带格式的: 字体: 倾斜
- 带格式的: 字体: 倾斜
- 带格式的: 字体: 倾斜

520 Qilian Mountains more adequately reflects the DSD characteristics in each class, unlike
521 when using the classification method of other sites with larger rainfall rates. More
522 importantly, the proposed classification of stratiform and convective rainfall can clearly
523 distinguish between the distribution of $\log_{10}N_w$ versus D_m in different rainfall types, for
524 which the dividing line (slope of -1.6 and intercept of 6.008) between stratiform and
525 convective rainfall has the same slope as the line (slope of -1.6 and intercept of 6.3)
526 given by Bringi et al (2003). Furthermore, according to this method, it can be easily
527 proven that convective events are more consistent with the not belong to the continental-
528 like cluster or maritime-like cluster, conforming to the unique precipitation
529 characteristics of the Qilian Mountains .

530 As mentioned above, the characteristics of DSD mainly describe diameters larger
531 than 0.2 mm, which is limited by the observation instruments being unable to detect
532 small drops of diameter less than 0.2 mm. Therefore, it is not a complete DSD, and the
533 number concentration of small drops of diameter less than 0.5 mm is underestimated.
534 Recent studies have been devoted to improving DSD observations in order to overcome
535 the limitations of disdrometers. A study by Thurai et al. (2017) obtained a more
536 complete DSD by splicing 2DVD and MPS (Meteorological Particle Spectrometer)
537 measurements to observe DSDs and developed a technology to reconstruct the drizzle-
538 mode DSD (Raupach et al., 2019), which a good presentation of the DSD of small
539 raindrops was provided, and important applications were highlighted.

540 5 Summary and conclusion

541 Based on six months of DSD data observed over the southern slopes, northern
542 slopes and interior of the Qilian Mountains, the characteristics and differences of DSD
543 were studied, and the $Z-R$ relationships of six sites were discussed. The main
544 conclusions can be summarized as follows:
545

- 546 1. For all rainfall events, the number concentrations of small and large raindrops in
547 the interior and on the southern slopes were greater than that on the northern slopes,
548 while midsize raindrops were less. The DSD of the interior of the mountains
549 showed great variability, mainly in terms of the $\log_{10}N_w$ and D_m (DSD parameters),
550 which was quite different to the case for the northern slopes.
- 551 2. The rainfall rates were divided into six categories based on the DSD characteristics:
552 C1, $R < 0.5$; C2, $0.5 \leq R < 2$; C3, $2 \leq R < 4$; C4, $4 \leq R < 6$; C5, $6 \leq R < 10$; and C6, > 10
553 mm h^{-1} . As the rainfall rate increased, the differences in number concentration of
554 each raindrop size became significantly larger, especially at the interior sites.
555 Besides, classes C5 and C6 made a relatively large contribution to the northern
556 slopes, with a greater probability of heavy precipitation events.
- 557 3. The dispersion degree of $\log_{10}N_w$ and D_m at the six sites was 8.3% and 10.0% for
558 stratiform rainfall and 10.4% and 23.4% for convective rainfall, respectively. It is
559 easier to increase the number concentration of large raindrops in the interior area
560 of the mountains during convective rainfall. Meanwhile, there is a greater increase
561 in the number concentration of raindrops over the northern slopes during
562 convective rainfall.

563 4. The dispersion degree of coefficient A and exponent b in the Z - R relationship for
564 the six sites was 42.5% and 10.7%, respectively. Overall, the Z - R relationships of
565 the ipsilateral sites were more consistent; and the A value of stratiform rainfall
566 increased from the southern slopes to northern slopes, while the opposite was true
567 for convective rainfall. The Z - R relationships in stratiform rainfall were similar
568 and generally underestimated by the $Z=200R^{1.6}$ model used for midlatitude
569 stratiform rainfall; and the Z - R relationships for convective precipitation varied
570 greatly at different *stationsites*, which were overestimated by $Z=300R^{1.4}$ at lower
571 rain rates values and underestimated at higher rain rates values.

572 This study reveals the microphysical variability of precipitation over the complex
573 topography of the arid and semi-arid regions of Northwest China, which can not only
574 improve local numerical simulations, but also provides a basis for further understanding
575 the differences in DSD characteristics formed at the mesoscale due to topographic
576 factors and the water vapor distribution, etc. This study holds importance as a basis for
577 the future implementation of weather modification techniques, which is of great
578 significance in solving the shortage of water resources in the arid and semi-arid regions.

579 *Data availability.* Disdrometer data used in this study are available by contacting the
580 authors.

581 *Author contributions.* WM conducted the detailed analysis; WZ provided financial
582 support and conceived the idea; MK collated the observation data; all the authors
583 contributed to the writing and revisions.

584 *Competing interests.* The authors declare that they have no conflict of interest.

585 **Acknowledgments**

586 The work was supported by Weather modification ability construction project of
587 Northwest China under grant No. ZQC-R18208 and The Second Tibetan Plateau
588 Comprehensive Scientific Expedition Grant No. 2019QZKK0104. Thanks are given to
589 Asi Zhang for her help in discussing some questions. The authors also thank reviewers
590 and editors for their helpful suggestion for this study

591 **References**

- 592 Adirosi, E., N. Roberto, M. Montopoli, E. Gorgucci, and L. Baldini, 2018: Influence of
593 disdrometer type on weather radar algorithms from measured DSD: Application
594 to Italian climatology. *Atmosphere*, 9, 360.
- 595 Angulo-Martínez, M., and A. Barros, 2015: Measurement uncertainty in rainfall kinetic
596 energy and intensity relationships for soil erosion studies: An evaluation using
597 PARSIVEL disdrometers in the Southern Appalachian Mountains.
598 *Geomorphology*, 228, 28-40.
- 599 Atlas, D., R. Srivastava, and R. S. Sekhon, 1973: Doppler radar characteristics of
600 precipitation at vertical incidence. *Reviews of Geophysics*, 11, 1-35.
- 601 Bringi, V., V. Chandrasekar, J. Hubbert, E. Gorgucci, W. Randeu, and M. Schoenhuber,
602 2003: Raindrop size distribution in different climatic regimes from disdrometer
603 and dual-polarized radar analysis. *Journal of the atmospheric sciences*, 60, 354-
604 365.
- 605 Campos, E., I. Zawadzki, M. Petitdidier, and W. Fernandez, 2006: Measurement of
606 raindrop size distributions in tropical rain at Costa Rica. *Journal of Hydrology*,
607 328, 98-109.
- 608 Chen, B., J. Yang, and J. Pu, 2013: Statistical characteristics of raindrop size
609 distribution in the Meiyu season observed in eastern China. *Journal of the*
610 *Meteorological Society of Japan. Ser. II*, 91, 215-227.
- 611 Dolan, B., B. Fuchs, S. Rutledge, E. Barnes, and E. Thompson, 2018: Primary modes
612 of global drop size distributions. *Journal of the Atmospheric Sciences*, 75, 1453-
613 1476.
- 614 Das, S., and A. Maitra, 2018: Characterization of tropical precipitation using drop size
615 distribution and rain rate-radar reflectivity relation. *Theoretical and applied*
616 *climatology*, 132, 275-286.
- 617 Fu, Z., and Coauthors, 2020: Statistical characteristics of raindrop size distributions and
618 parameters in Central China during the Meiyu seasons. *Journal of Geophysical*
619 *Research: Atmospheres*, 125, e2019JD031954.
- 620 Fulton, R. A., J. P. Breidenbach, D.-J. Seo, D. A. Miller, and T. O'Bannon, 1998: The
621 WSR-88D rainfall algorithm. *Weather and forecasting*, 13, 377-395.
- 622 Geoffroy, O., A. Siebesma, and F. Burnet, 2014: Characteristics of the raindrop
623 distributions in RICO shallow cumulus. *Atmospheric Chemistry and Physics*, 14,
624 10897-10909.
- 625 Ghada, W., A. Buras, M. Lüpke, C. Schunk, and A. Menzel, 2018: Rain microstructure
626 parameters vary with large-scale weather conditions in Lausanne, Switzerland.
627 *Remote Sensing*, 10, 811.
- 628 Giannetti, F., and Coauthors, 2017: Real-time rain rate evaluation via satellite downlink
629 signal attenuation measurement. *Sensors*, 17, 1864.
- 630 Gou, X., F. Chen, M. Yang, J. Li, J. Peng, and L. Jin, 2005: Climatic response of thick
631 leaf spruce (*Picea crassifolia*) tree-ring width at different elevations over Qilian
632 Mountains, northwestern China. *Journal of Arid Environments*, 61, 513-524.

633 Guyot, A., Pudashine, J., Protat, A., Uijlenhoet, R., Pauwels, V., Seed, A., and Walker,
634 J. P., 2019: Effect of disdrometer type on rain drop size distribution
635 characterisation: A new dataset for south-eastern Australia. *Hydrology and Earth
636 System Sciences*, 23, 4737-4761.

637 Jash, D., E. Resmi, C. Unnikrishnan, R. Sumesh, T. Sreekanth, N. Sukumar, and K.
638 Ramachandran, 2019: Variation in rain drop size distribution and rain integral
639 parameters during southwest monsoon over a tropical station: An inter-comparison
640 of disdrometer and Micro Rain Radar. *Atmospheric Research*, 217, 24-36.

641 Jaffrain, J., and Berne, A., 2011: Experimental quantification of the sampling
642 uncertainty associated with measurements from PARSIVEL disdrometers. *Journal
643 of Hydrometeorology*, 12, 352-370.

644 Kruger, A., and W. F. Krajewski, 2002: Two-dimensional video disdrometer: A
645 description. *Journal of Atmospheric and Oceanic Technology*, 19, 602-617.

646 Le Loh, J., D.-I. Lee, and C.-H. You, 2019: Inter-comparison of DSDs between
647 Jincheon and Miryang at South Korea. *Atmospheric Research*, 227, 52-65.

648 Li, Z., and Coauthors, 2019: Climate background, relative rate, and runoff effect of
649 multiphase water transformation in Qilian Mountains, the third pole region.
650 *Science of The Total Environment*, 663, 315-328.

651 Lim, Y. S., J. K. Kim, J. W. Kim, B. I. Park, and M. S. Kim, 2015: Analysis of the
652 relationship between the kinetic energy and intensity of rainfall in Daejeon, Korea.
653 *Quaternary International*, 384, 107-117.

654 Ma, L., L. Zhao, D. Yang, Y. Xiao, L. Zhang, and Y. Qiao, 2019a: Analysis of Raindrop
655 Size Distribution Characteristics in Permafrost Regions of the Qinghai-Tibet
656 Plateau Based on New Quality Control Scheme. *Water*, 11, 2265.

657 Ma, Y., G. Ni, C. V. Chandra, F. Tian, and H. Chen, 2019b: Statistical characteristics of
658 raindrop size distribution during rainy seasons in the Beijing urban area and
659 implications for radar rainfall estimation. *Hydrology and Earth System Sciences*,
660 23, 4153-4170.

661 Marshall, J. S., 1948: The distribution of raindrops with size. *J. meteor.*, 5, 165-166.

662 McFarquhar, G. M., T.-L. Hsieh, M. Freer, J. Mascio, and B. F. Jewett, 2015: The
663 characterization of ice hydrometeor gamma size distributions as volumes in N_0 -
664 λ - μ phase space: Implications for microphysical process modeling. *Journal of
665 Atmospheric Sciences*, 72, 892-909.

666 Narayana Rao, T., N. Kirankumar, B. Radhakrishna, and D. Narayana Rao, 2006: On
667 the variability of the shape-slope parameter relations of the gamma raindrop size
668 distribution model. *Geophysical research letters*, 33.

669 Protat, A., and Coauthors, 2019: The latitudinal variability of oceanic rainfall properties
670 and its implication for satellite retrievals: 1. Drop size distribution properties.
671 *Journal of Geophysical Research: Atmospheres*, 124, 13291-13311.

672 Pu, K., X. Liu, Y. Wu, S. Hu, L. Liu, and T. Gao, 2020: A comparison study
673 of raindrop size distribution among five sites at the urban scale during the
674 East Asian rainy season. *Journal of Hydrology*, 590, 125500, <https://doi.org/>

675 g/10.1016/j.jhydrol.2020.125500.

676 Penide, G., A. Protat, V. V. Kumar, and P. T. May, 2013: Comparison of two
677 convective/stratiform precipitation classification techniques: Radar reflectivity
678 texture versus drop size distribution-based approach. *Journal of Atmospheric and*
679 *Oceanic Technology*, 30, 2788-2797.

680 Qin, Y., H. Lei, D. Yang, B. Gao, Y. Wang, Z. Cong, and W. Fan, 2016: Long-term
681 change in the depth of seasonally frozen ground and its ecohydrological impacts
682 in the Qilian Mountains, northeastern Tibetan Plateau. *Journal of Hydrology*, 542,
683 204-221.

684 Rincon, R. F., and R. H. Lang, 2002: Microwave link dual-wavelength measurements
685 of path-average attenuation for the estimation of drop size distributions and rainfall.
686 *IEEE Transactions on geoscience and remote sensing*, 40, 760-770.

687 Raupach, T. H., M. Thurai, V. Bringi, and A. Berne, 2019: Reconstructing the drizzle
688 mode of the raindrop size distribution using double-moment normalization.
689 *Journal of Applied Meteorology and Climatology*, 58, 145-164.

690 Seela, B. K., J. Janapati, P. L. Lin, K. K. Reddy, R. Shirooka, and P. K. Wang, 2017: A
691 comparison study of summer season raindrop size distribution between Palau and
692 Taiwan, two islands in western Pacific. *Journal of Geophysical Research: Atmospheres*, 122, 11,787-711,805.

694 Smith, J. A., E. Hui, M. Steiner, M. L. Baeck, W. F. Krajewski, and A. A. Ntekos,
695 2009: Variability of rainfall rate and raindrop size distributions in heavy rain.
696 *Water Resources Research*, 45.

697 Thurai, M., P. Gatlin, and V. Bringi, 2016: Separating stratiform and convective rain
698 types based on the drop size distribution characteristics using 2D video
699 disdrometer data. *Atmospheric Research*, 169, 416-423.

700 Thurai, M., P. Gatlin, V. Bringi, W. Petersen, P. Kennedy, B. Notaroš, and L. Carey,
701 2017: Toward completing the raindrop size spectrum: Case studies involving 2D-
702 video disdrometer, droplet spectrometer, and polarimetric radar measurements.
703 *Journal of Applied Meteorology and Climatology*, 56, 877-896.

704 Testud, J., S. Oury, R. A. Black, P. Amayenc, and X. Dou, 2001: The concept of
705 “normalized” distribution to describe raindrop spectra: A tool for cloud physics
706 and cloud remote sensing. *Journal of Applied Meteorology*, 40, 1118-1140.

707 Tian, H., T. Yang, and Q. Liu, 2014: Climate change and glacier area shrinkage in the
708 Qilian mountains, China, from 1956 to 2010. *Annals of Glaciology*, 55, 187-197.

709 [Tokay A, Wolff D B, Petersen W A, 2014. Evaluation of the New Version of the Laser-](#)
710 [Optical Disdrometer, OTT Parsivel². *Journal of atmospheric and oceanic*](#)
711 [technology, 31, 1276-1288.](#)

712 Ulbrich C W., 1983: Natural variations in the analytical form of the raindrop size
713 distribution. *Journal of climate and applied meteorology*, 22, 1764-1775.

714 Wainwright, C. E., D. T. Dawson, M. Xue, and G. Zhang, 2014: Diagnosing the
715 intercept parameters of the exponential drop size distributions in a single-moment
716 microphysics scheme and impact on supercell storm simulations. *Journal of*

带格式的: 字体: Times New Roman, 字体颜色: 自动设置

带格式的: 字体: Times New Roman, 小四, 字体颜色: 自动设置, 上标

717 Applied Meteorology and Climatology, 53, 2072-2090.
718 Wang, Y., J. Zheng, Z. Cheng, and B. Wang, 2020: Characteristics of Raindrop Size
719 Distribution on the Eastern Slope of the Tibetan Plateau in Summer. Atmosphere,
720 11, 562.
721 Wu, Y., and L. Liu, 2017: Statistical characteristics of raindrop size distribution in the
722 Tibetan Plateau and southern China. Advances in Atmospheric Sciences, 34, 727-
723 736.
724 Yang, L., J. Smith, M. L. Baeck, B. Smith, F. Tian, and D. Niyogi, 2016: Structure and
725 evolution of flash flood producing storms in a small urban watershed. Journal of
726 Geophysical Research: Atmospheres, 121, 3139-3152.
727 Zhang, A., and Coauthors, 2019: Statistical characteristics of raindrop size distribution
728 in the monsoon season observed in southern China. Remote Sensing, 11, 432.
729 Zhao, P., and Coauthors, 2019: The Tibetan Plateau surface-atmosphere coupling
730 system and its weather and climate effects: The Third Tibetan Plateau Atmospheric
731 Science Experiment. Journal of Meteorological Research, 33, 375-399.
732 Zeng, Y., and Coauthors, 2021: Statistical Characteristics of Raindrop Size Distribution
733 during Rainy Seasons in Northwest China. Advances in Meteorology, 2021.
734